Soft Matter

Comparative evaluation of melt- vs. solution-printed poly(��-caprolactone)/hydroxyapatite scaffolds for bone tissue engineering applications

Journal:	*Soft Matter*
Manuscript ID	SM-ART-10-2024-001197.R1
Article Type:	Paper
Date Submitted by the Author:	18-Nov-2024
Complete List of Authors:	Gharacheh, Hadis; New Jersey Institute of Technology Newark College of Engineering Abaci, Alperen; New Jersey Institute of Technology Newark College of Engineering Alkhoury, Keven; New Jersey Institute of Technology Newark College of Engineering Choudhury, Ediha; New Jersey Institute of Technology Newark College of Engineering Liaw, Chya-Yan; New Jersey Institute of Technology Newark College of Engineering, Chemical and Materials Engineering Chester, Shawn; New Jersey Institute of Technology Guvendiren, Murat; New Jersey Institute of Technology Newark College of Engineering,

ARTICLE

Comparative evaluation of melt- vs. solution-printed poly(ε-caprolactone)/hydroxyapatite scaffolds for bone tissue engineering applications

Received 00th January 20xx,
Accepted 00th January 20xx

DOI: 10.1039/x0xx00000x

Hadis Gharacheh,[#a] Alperen Abaci,[#a] Keven Alkhoury,[b] Ediha Choudhury,[c] Chya-Yan Liaw,[a] Shawn A. Chester,[b] and Murat Guvendiren*[ac]

Material extrusion-based three-dimensional (3D) printing is a widely used manufacturing technology for fabricating scaffolds and devices in bone tissue engineering (BTE). This technique involves two fundamentally different extrusion approaches: solution-based and melt-based printing. In solution-based printing, a polymer solution is extruded and solidifies via solvent evaporation, whereas in melt-based printing, the polymer is melted at elevated temperatures and solidifies as it cools post-extrusion. Solution-based printing can also be enhanced to generate micro/nano-scale porosity through phase separation by printing the solution into a nonsolvent bath. The choice of printing method directly affects scaffold properties and the biological response of stem cells. In this study, we selected polycaprolactone (PCL), a biodegradable polymer frequently used in BTE, blended with hydroxyapatite (HA) nanoparticles, a bioceramic known for promoting bone formation, to investigate the effects of printing approach on scaffold properties and performance in vitro using human mesenchymal stem cells (hMSCs). Our results showed that while both printing methods produced scaffolds with similar strut and overall scaffold dimensions, solvent-based printing resulted in porous struts, higher surface roughness, lower stiffness, and increased crystallinity compared to melt-based printing. Although stem cell viability and proliferation were not significantly influenced by the printing approach, melt-printed scaffolds promoted a more spread morphology and exhibited pronounced vinculin staining. Furthermore, composite scaffolds outperformed their neat counterparts, with melt-printed composite scaffolds significantly enhancing bone formation. This study highlights the critical role of the printing process in determining scaffold properties and performance, providing valuable insights for optimizing scaffold design in BTE.

Introduction

Bone tissue engineering (BTE) represents a promising frontier in regenerative medicine, aiming to develop three-dimensional (3D) scaffolds that mimic the native extracellular matrix (ECM) of bone tissue.[1, 2] These scaffolds harness the bone's intrinsic regenerative capacity by providing a mechanically stable framework that captures cells and biological cues from the defect site to promote new tissue formation.[3-6] The scaffolds create a supportive microenvironment for cell migration, adhesion, proliferation, and differentiation, or preservation of the cell phenotype.

Although conventional and advanced manufacturing approaches – including electrospinning,[7] freeze-drying,[8] phase separation,[9] gas foaming,[10] and particulate leaching[11] – have enabled the fabrication of 3D scaffolds for BTE, 3D printing (additive manufacturing) has revolutionized scaffold fabrication.[12-16] It allows precise control over scaffold design, porosity, mechanical properties, and biomaterial composition.[17-21] 3D printing technologies, particularly polymer filament printing (commonly known as fused deposition modeling or FDM, trademarked by Stratasys),[22-24] direct ink writing (DIW),[25-27] stereolithography (SLA),[28, 29] digital light processing (DLP),[30, 31] and selective laser sintering (SLS),[32, 33] have enabled the fabrication of highly customizable, patient-specific scaffolds to meet specialized clinical needs.[34-37] Among these, material extrusion-based 3D printing is widely used for BTE due to the availability of printers, ease of operation, and the ability to process commonly utilized biodegradable polymers and their composites.[38-40]

Melt-based and solvent-based printing are the two primary extrusion-based 3D printing technologies. In melt-based printing, the polymer is loaded as a pellet or powder, melted at a temperature (T_p) slightly above its melting temperature (T_m), but usually below 250°C for most commercial printers.[41] The melt viscosity at T_p should be below 10^6 mPa·s to allow flow under applied pressure.[41] Common biodegradable polymers like polylactic acid (PLA) and polycaprolactone (PCL) are printed at ~180°C (T_m = 160°C) and ~80°C (T_m = 60°C), respectively.[41-43] The polymer must rapidly transition from melt to solid, ensuring quick solidification after extrusion.[42] Prolonged exposure of

[a] Otto H. York Department of Chemical and Materials Engineering, New Jersey Institute of Technology, Newark, NJ 07102, USA
[b] Department of Mechanical & Industrial Engineering, New Jersey Institute of Technology, Newark, NJ 07102, USA.
[c] Department of Biomedical Engineering, New Jersey Institute of Technology, Newark, NJ 07102, USA
[#] Contributed equally.
† Electronic Supplementary Information (ESI) available: [details of any supplementary information available should be included here]. See DOI: 10.1039/x0xx00000x

biodegradable polymers to high temperatures and pressures may lead to polymer degradation and denaturation of incorporated bioactive cues.[42, 44]

In solvent-based 3D printing, the biodegradable polymer is dissolved in a volatile solvent, and the concentration is adjusted to control solution viscosity (1-10^4 Pa·s) for extrusion.[26, 45, 46] As the solution is printed, the solvent evaporates, forming a solid polymer strut. PLA (7.5-30 wt% in dichloromethane (DCM))[45, 47, 48] and PCL (7.5-40 wt% in 1,1,1,3,3,3-hexafluoro-2-propanol (HFIP), DCM or acetone)[26, 49, 50] have been used to create scaffolds via this method. This approach allows printing at room temperature, which is useful for processing polymers unsuitable for melt-based printers, as well as for hydrogels, highly filled polymer composites (slurries), and resins.[50-52] Both approaches produce 3D scaffolds with solid struts, and the spacing between struts can be adjusted to create macroporosity, which is essential for cell infiltration and tissue growth.

There is growing interest in creating (macro)porous scaffolds with micro- and/or nanoporous struts to better mimic the cancellous bone structure.[53] In this regard, solvent-based printing is combined with nonsolvent-induced phase separation (NIPS) process, known as solvent exchange deposition modeling (SEDM)[54, 55] or NIPS-based 3D printing.[53, 56, 57] In this method, polymer solution is printed into a nonsolvent liquid or vapor, and the solvent exchange induces phase separation followed by precipitation. For instance, 3D macrochanneled PCL scaffolds with highly porous frameworks (struts) have been fabricated by printing PCL/tetrahydrofuran (THF) solution (14-22 wt.%) into an ethanol (EtOH) bath.[57] Mechanical properties of the scaffolds increased with an increase in PCL concentration due to a decrease in the overall strut porosity.[57] PCL/THF scaffolds exposed to humidity develop surface porosity with tunable pore sizes controlled by the humidity level (60-80%), such that the average pore size and density increased with the humidity level.[58] Macro/nano-porous collagen scaffolds composed of nanofibrous collagen filaments have been created through a pH-dependent precipitation by deposited collagen solution (pH~3.4) in a coagulation bath (pH~10).[59] Similarly, printing of polylactic-co-glycolic acid (PLGA)/tetraglycol (TG) solution in water produces microporous or hallow struts,[60] while PLGA/N-methyl pyrrolidone (NMP) solution (40% w/v) has been printed into EtOH to create flexible skin substitute scaffolds.[54] Additionally, cellulose scaffolds printed from dimethyl sulfoxide (DMSO) and tetrabutylammonium hydroxide (TBAH) solution are solvent-exchanged with deionized (DI) water after printing.[55]

NIPS-based 3D printing has been used to create PCL/HA composite scaffolds with various HA contents (0-20 wt%) for bone tissue regeneration.[56] Scaffolds showed consistent overall porosity (~78 vol %) and (strut) pore size (~2.8 μm), but mechanical properties improved with increased HA content.[56] Aydin et al. also investigated the microstructural organization of PCL/hydroxyapatite (HA) bone scaffolds using the NIPS process, finding that pore size increased with HA content (0-20 wt%) for manually made PCL/HA composite films.[61] Moreover, PCL-calcium phosphate (CaP) composite scaffolds with microporous surfaces have been fabricated by printing PCL-CaP solution in acetone into water.[62] The incorporation of CaP did not hinder the formation of microporous structures but enhanced the scaffolds' biocompatibility, apatite-forming ability, and mechanical properties.[62]

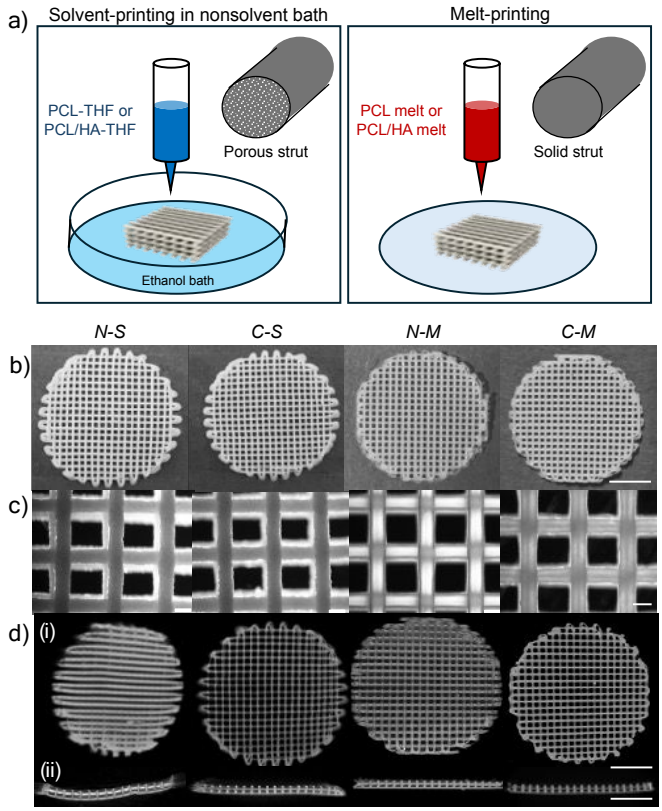

Figure 1. a) Schematics of solution-printing (*S*) within nonsolvent bath and melt-printing (*M*). b) Pictures (top view), c) optical images (top view), d) micro-CT images ((i) top and (ii) cross-section) of neat PCL (*N*) and PCL/HA composite (*C*) scaffolds fabricated via solution-printing (*N-S and C-S*) and melt-printing (*N-M and C-M*). Scale bars are 5 mm (b, d), and 200 μm (c).

The selection of the printing method significantly affects scaffold properties, including mechanical behaviour, overall porosity, surface roughness, and crystallinity, which are critical for determining the scaffold's suitability for BTE. In this study, we present a systematic comparison of scaffolds fabricated using melt-based printing and solvent-based printing combined with the NIPS process. PCL was chosen as the base material due to its versatility and widespread use in 3D-printed BTE scaffolds.[63-67] Hydroxyapatite (HA) particles were incorporated to promote bone regeneration, as PCL is commonly blended with bioceramic fillers, such as HA and tricalcium phosphate (TCP), to improve scaffold bioactivity and mechanical properties.[68-70] We examine the structural, thermal, and mechanical properties of the scaffolds, alongside the osteogenic differentiation of seeded stem cells, to evaluate the scaffold's potential for BTE applications. This work uniquely contrasts solution-based and melt-based extrusion printing methods in fabricating scaffolds for bone tissue engineering, revealing how these approaches influence scaffold porosity, mechanical properties, and human

mesenchymal stem cell behaviour, which has been minimally explored in such detail.

Table 1 Ink formulations and printing conditions for neat (*N*) and composite (*C*) with solution- (*S*) and melt-printing (*M*)

	PCL (wt.%)	HA (wt.%)	Solvent	Bath	T_p (°C)	*P* (kPa)	v (mm/s)
N-S	100	0	THF	EtOH	25	172	15
C-S	80	20	THF	EtOH	25	172	15
N-M	100	0	-	-	150	690	5
C-M	80	20	-	-	180	690	1

T_p: print temperature; *P*: print pressure; v: print speed

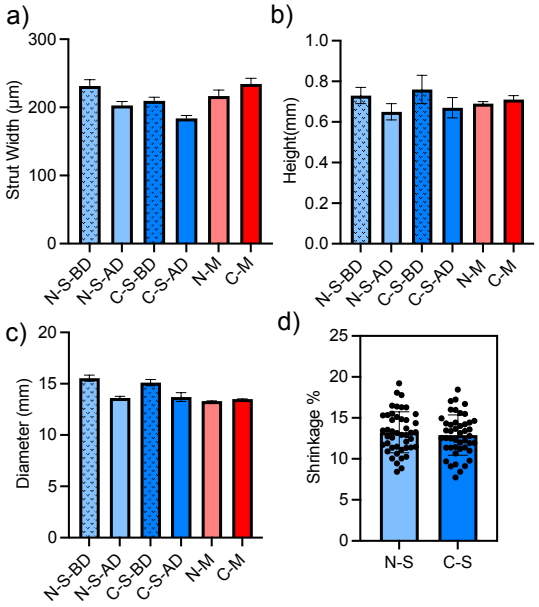

Figure 2. Characterization of scaffold parameters including a) strut width, b) scaffold height, c) scaffold diameter, and d) percent shrinkage for solution-printed samples. Solution-printed neat and composite scaffolds are denoted as *N-S* and *C-S* with BD and AD referring before and after drying, respectively. *N-M* and *C-M* refer to melt-printed neat and composite scaffolds. Data were presented as mean ± sd. Statistical analysis was performed using one-way analysis of variance (ANOVA).

Results and discussion

Fabrication of scaffolds

Neat PCL (*N*) and PCL/HA composite (*C*) scaffolds were fabricated by melt-based printing (*M*) and solution-based printing (*S*) combined with NIPS process (**Figure 1a**). The printability of the ink formulations dictates scaffolds' structural uniformity and mechanical behavior.[71] As confirmed with optical and micro-CT images **(Figure 1b-d)**, 3D scaffolds were successfully printed using the optimum printing conditions for each formulation and printing method **(Table 1)**. Disk shaped scaffolds (14 mm in diameter) were constructed as 4 layers with each layer composed of linear struts but rotating 90° in each repeating layer. The average strut size (190-230 µm), scaffold height (0.68-0.72 mm) and scaffold diameter (13-15 mm) are given in **Figure 2a-c**. There were slight variations in these parameters for *S* samples after drying due to shrinkage (~13% in strut diameter) **Figure 2d**.

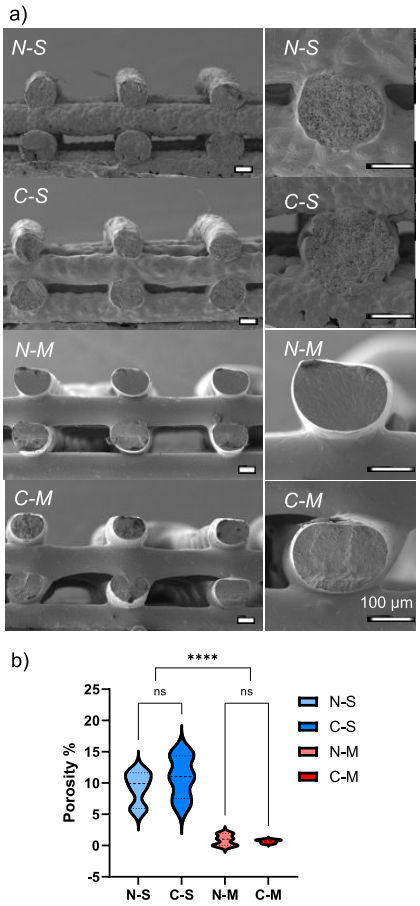

Figure 3. a) Representative SEM images of neat (*N*) and composite (C) scaffolds fabricated via solution-printing (*S*) and melt-printing (*M*). b) Percent porosity of struts. Statistical analysis was performed using one-way analysis of variance (ANOVA). ****p < 0.0001 and ns: no significant difference.

Characterization of scaffolds

Surface morphology. The surface morphology of a scaffold plays a key role in regulating cell attachment, migration, and shape, as well as differentiation.[72-75] SEM images showed solid struts (~0.2% porosity), with smooth surfaces for *M* as compared to *S* with porous struts (~10% porosity) with surface irregularities **(Figure 3)**. AFM scans revealed that the *S* scaffolds exhibited significantly higher surface roughness as compared to *M* counterparts, with no significant difference between neat and composite scaffolds despite slight increase in roughness for composite scaffolds **(Figure 4)**. In **Figure 4b and c**, roughness parameters – the arithmetic average of surface height deviations (R_a) and the root-mean-square average of height deviations (R_q), were plotted for quantitative comparison. R_a values were 50.5 ± 9.6 nm and 97 ± 9.1 nm for *N-S* and *C-S*, and 14 ± 0.6 nm and 26 ± 2.4 nm for *N-M* and *C-M* samples. R_q values were 78 ± 12.6 nm and 122 ± 12.5 nm for *N-S* and *C-S*, 19 ± 1.2 nm and 34 ± 2.6 nm for *N-M* and *C-M* samples. Surface roughness is known to be a regulating factor for stem cell behaviour,[73, 74] and the significantly higher values observed for solution-printed

scaffolds could impact cellular behaviour via controlling cell shape.

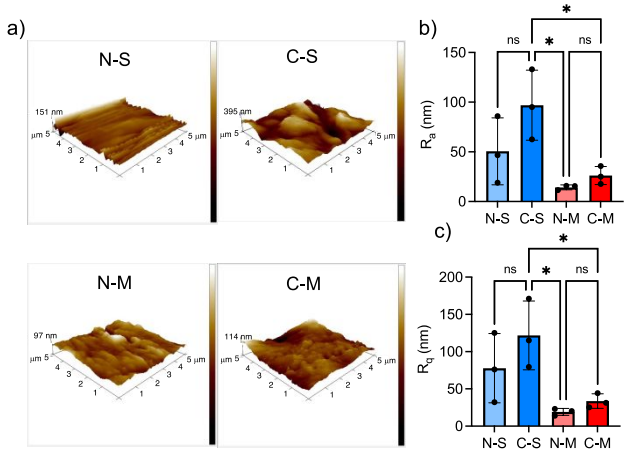

Figure 4. a) Representative AFM images of struts from neat (*N*) and composite (*C*) scaffolds fabricated via solution-printing (*S*) and melt-printing (*M*). b, c) Corresponding roughness parameters: b) the arithmetic average of surface height deviations (R_a) and (c) the root-mean-square average of height deviations (R_q). Data were presented as mean ± sd. Statistical analysis was performed using one-way analysis of variance (ANOVA). *p < 0.05, and ns: no significance (n=3).

Thermal behaviour. Thermal gravimetric analysis (TGA) was used to confirm the HA composition of the 3D printed scaffolds, which is a determining factor for their mechanical behaviour and bioactivity towards cells.[70, 76, 77] In this regard, complete mass loss was achieved for neat scaffolds (*N-M* and *N-S*) whereas 20% of the initial mass remained for composite scaffolds (*C-M* and *C-S*) after thermal degradation of polymers, which corresponds to the HA loading **(Figure 5a)**. Neat scaffolds (*N-M* and *N-S*) showed a sharp degradation step starting at ~350˚C which shifted to ~280˚C for composite scaffolds (*C-M* and *C-S*). Confirming our results, PCL/HA composites have been reported to show thermal degradation starting at ~250˚C.[68, 70, 76] For the solvent-based printed samples, TGA analysis confirmed that the solvent was completely removed (or reduced to an insignificant amount). If the solvent is not removed properly, solvent-printed samples show an initial gradual degradation, corresponding to solvent evaporation within the temperature range of the boiling temperature of the solvent, followed by a sharp decrease corresponding to the polymer degradation.[78] In our case both melt and solvent printed samples showed a single sharp decrease, and we did not see any gradual decrease in the range of 66˚C to 78˚C corresponding to the boiling point of THF and EtOH, respectively.

Differential scanning calorimetry (DSC) is used to investigate the thermal characteristics of the scaffolds, in which the first heating cycle represents the direct effects of the printing process whereas the second heating cycle shows the material properties **(Figure 5b-d, Table 2)**. No significant difference in T_m was observed between samples, yet T_m was higher in the first heating cycle (T_m = 61-62 ˚C) compared to that of the second one (T_m = 57-58 ˚C). Similarly, the degree of crystallinity, χ_c(%), was significantly higher (~2x) in the first heating cycle, and solution-printed samples showed significantly higher χ_c with *C-S* (~81%) higher than *N-S* (~75%) compared to melt-printed samples (~57% and ~65% for *C-M* and *N-M*, respectively). Solvent-printed samples crystallized at room temperature whereas melt-printed samples crystallized during cooling from high temperature to room temperature. Increased crystallinity for solvent-printed samples could be explained by improved polymer chain mobility in the presence of solvent combined with chain confinement and alignment due to shear induced flow in the nozzle. The crystallite formation is enhanced in the presence of HA nanoparticles as they are known to act as nucleation sites during crystallization.[78] The overall decrease in crystallinity in the second heating cycle is due to erased processing history. Supporting our findings, it has been shown that shear flow during extrusion-based printing led to a higher degree of crystallization due to chain alignment providing nucleation sites for crystal formation.[79-81]

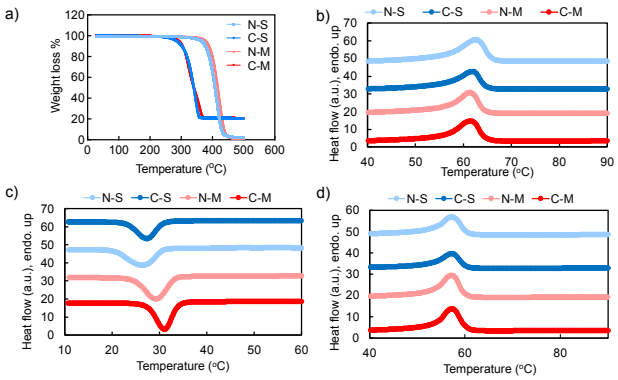

Figure 5. Thermal behaviour of the printed scaffolds: neat (*N*) and composite (*C*) scaffolds fabricated via solution-printing (*S*) and melt-printing (*M*): a) TGA curves, b) DSC first heating curves, c) DSC cooling curves, and d) DSC second heating curves.

Table 2 The melting temperature, heat of melting and degree of crystallinity for neat (*N*) and composite (*C*) solvent printed (*N-S* and *C-S*) and melt-printed (*N-M* and *C-M*) samples

	1st Heating			2nd Heating		
Sample	T_m (°C)	ΔH_m ($J \cdot g^{-1}$)	χ_c (%)	T_m (°C)	ΔH_m ($J \cdot g^{-1}$)	χ_c (%)
N-S	63±0.1	102±1.3	75±1	57±0.1	52±0.0	38±0.0
C-S	63±0.5	88±6.3	81±6	58±0.2	48±2.9	44±2.7
N-M	62±0.3	77±0.1	57±1	57±0.1	52±1.4	38±1.0
C-M	62±0.2	71±0.5	65±1	57±0.1	48±1.2	44±1.1

Mechanical behaviour. Cells are known to sense the stiffness of their surrounding matrix and, in response, regulate functions such as contraction, shape, migration, proliferation, and differentiation.[82-87] Generally, increased stiffness is associated with enhanced osteogenic differentiation.[49, 78, 88] Since our scaffolds consist of 3D-printed struts on which cells reside, the stiffness of these struts directly influences stem cell behaviour. To evaluate the impact of the 3D printing process on stiffness (tensile modulus, *E*) and thus stem cell function, we measured the *E* values of the struts **(Figure 6)**.

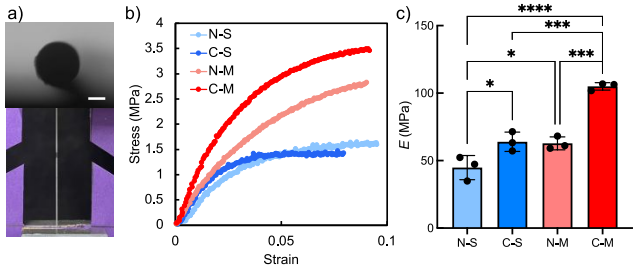

Figure 6. Mechanical behaviour of printed filaments: a) Pictures of typical sample cross-section view (top) and tensile test setup (bottom) with scale bar = 200 mm, b) representative stress-strain curves, and c) Young's modulus values. In (c), data were presented as mean ± sd (n=3). Statistical analysis was performed using one-way analysis of variance (ANOVA). Differences were considered significant at *p < 0.05, ***p < 0.001 and ****p < 0.0001.

The stress-strain diagrams **(Figure 6b)** indicated that the melt-printed samples (*N-M* and *C-M*) exhibited much steeper curves in the elastic deformation region (<0.02% strain) and reached higher stress values before necking, with *C-M* >> *N-M*. The *E* was substantially higher for *C-M* (105 ± 2.2 MPa) compared to *N-M* (62 ± 3.8 MPa) **(Figure 6c)**, and slightly higher for *C-S* (64 ± 1.9 MPa) compared to *N-S* (45 ± 2.4 MPa). It is well established that the incorporation of bioceramic particles, such as HA, enhances the stiffness of 3D-printed polymers,[24] which was more pronounced in the melt-printed samples. However, porosity is known to have a detrimental effect on stiffness,[89, 90] and we believe that this effect dominated in the solution-printed samples.

Stem cell response. Human mesenchymal stem cells (hMSCs) were cultured on the scaffolds to investigate the effects of the 3D printing process (*M* vs. *S*) and the presence of HA particles (*N* vs. *C*) on cell growth and osteogenic differentiation. AlamarBlue and PicoGreen assays were performed to assess cell viability and proliferation over a 14-day culture period in growth media **(Figure 7)**. Overall, cell metabolic activity significantly increased between Day 1 and Day 4, as indicated by a rise in mean intensity, and then stabilized after Day 4 across all sample groups. DNA content also significantly increased with time, reflecting cell proliferation. No significant differences were observed between the groups at any time point.

Multiphoton confocal images of the hMSCs (F-actin in red, nuclei in blue) at Day 1 and Day 7 are shown in **Figure 7c**. The F-actin filaments aligned with the printed struts, an alignment that became more pronounced by Day 7. Cell area was significantly larger on melt-printed samples (2500 ± 16.1 µm² for *N-M* and 2700 ± 24.8 µm² for *C-M*) compared to solution-printed samples (1700 ± 13.2 µm² for *N-S* and 1200 ± 9.7 µm² for *C-S*), with no significant difference between *N* and *C* scaffolds within each group (**Figure 7d)**. However, the cell aspect ratio was higher for solution-printed samples (3.4 ± 1.9 for *N-S* and 3.1 ± 1.7 for *C-S*) than for melt-printed samples (2.4 ± 1.3 for *N-M* and 2.5 ± 0.9 for *C-M*), again with no significant differences between *N* and *C* samples (**Figure 7e)**. In addition, cells on melt-printed samples showed mature vinculin (focal adhesion marker) patches as compared to diffused staining for solution-printed samples at day 7 **(Figure 7f)**.

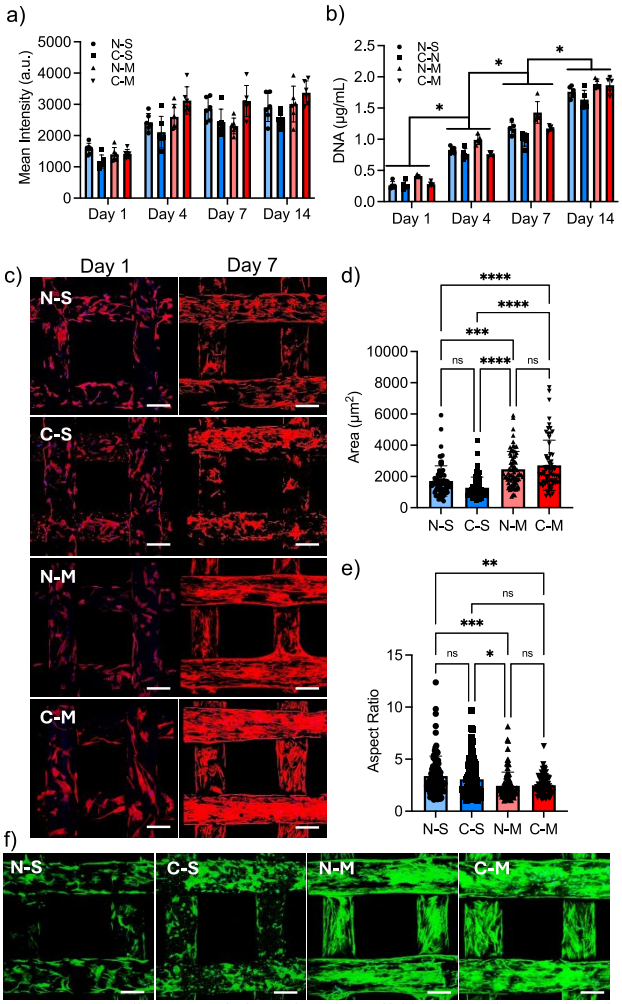

Figure 7. Stem cell response during culture in scaffolds (neat and composite solution-printed (*N-S and C-S*) and melt-printed (*N-M* and *C-M*) scaffolds): a) mean intensity obtained from AlamarBlue assay, b) DNA content obtained from Picogreen assay, c) confocal images of hMSCs cultured on scaffolds at Day 1 and Day 7 (F-actin: red, nuclei: blue), scale bar: 200 mm, d) cell area, e) cell aspect ratio, and f) confocal images of hMSCs immunostained for vinculin (green) at day 14, scale bar 200 mm. Data in (a, b, d, and e) were presented as mean ± sd (n = 6 for a and b, and n ≥ 60 for d and e). Statistical analysis was performed using one-way analysis of variance (ANOVA). Differences were considered significant at *p < 0.05, **p < 0.01, ***p < 0.001 and ****p < 0.0001, ns: no significant difference.

In summary, cells were bulkier and less elongated on melt-printed samples with more pronounced focal adhesion compared to solution-printed samples. This could be attributed to the combined effect of higher surface roughness and lower modulus observed in solution-printed samples. The presence of HA did not notably affect cell behaviour, likely because the particles were fully embedded in the printed struts, as shown in the SEM images **(Figure 3)**. When HA particles are coated onto scaffold surfaces, they typically have a more direct impact on cell behaviour.[91]

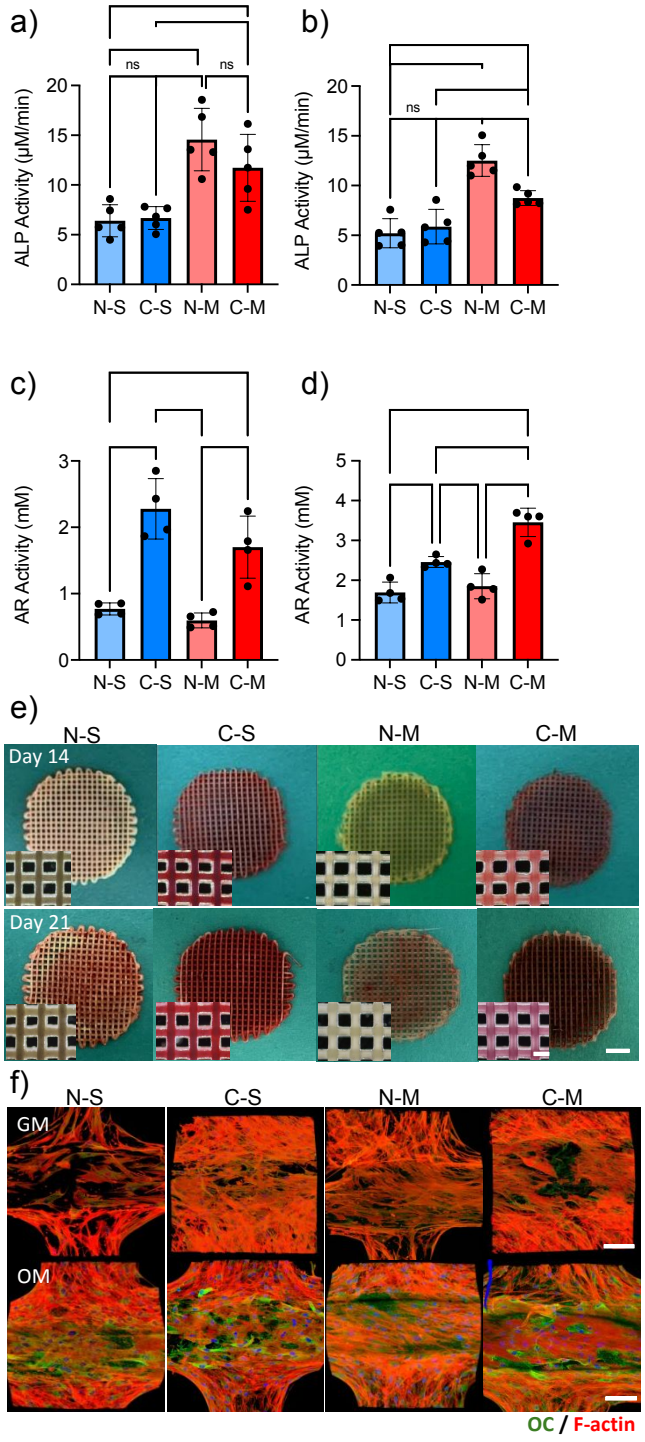

Figure 8. Characterization of bone formation: a, b) alkaline phosphatase (ALP) activity of hMSCs at day 14 (a) and day 21 (b); c, d) calcium deposition at day 14 (c) and day 21 (d); f) optical and bright field images (insets) of hMSCs stained for alizarin red (AR) at day 14 and 21, scale bars: 500 μm for optical images and 200 μm for insets, and f) confocal images of hMSCs cultured in growth media (GM) and osteogenic induction media (OM) for 21 days and stained for osteocalcin (OC, green) and F-actin (red), scale bars: 200 mm. In (a-d), data were presented as mean ± sd (n = 6). Statistical analysis was performed using one-way analysis of variance (ANOVA). Differences were considered significant at *p < 0.05, **p < 0.01, ***p < 0.001 and ****p < 0.0001, ns: no significant difference.

In vitro bone formation. Osteogenic differentiation of hMSCs was assessed through alkaline phosphatase (ALP) activity, calcium deposition, and osteocalcin (OC) immunostaining. The cells were seeded on scaffolds and cultured in growth media (GM) for 7 days, followed by 14 days in osteogenic media (OM), totaling 21 days of culture.

ALP activity **(Figure 8a, b)** was significantly higher for hMSCs cultured on *M* samples, with increases of 1.5x for *C* and 2.2x for *N*. No significant change in ALP activity was observed between Day 14 and 21. While ALP upregulation is indicative of bone formation and early osteogenic differentiation, its lack of specificity means it should not be the sole marker of osteogenesis.

Calcium deposition was measured using alizarin red (AR) activity **(Figure 8c-e).** At Day 14 and Day 21, calcium deposition was significantly higher on *C* scaffolds than on *N* scaffolds, approximately 2.8x higher for *S* and *M* scaffolds at Day 14, decreasing to 1.5x for *S* and 2x for *M* by Day 21. No significant difference in calcium deposition was observed between *C-S* and *C-M* at Day 14, but *C-M* had 1.3x higher calcium levels by Day 21. Calcium deposition increased over time in *N-S* and *N-M* scaffolds, though there was no significant difference between scaffold types at each time point. hMSCs showed positive OC immunostaining staining (green) in OM at Day 14, while staining was undetectable or insignificant in GM **(Figure 8f)**.

In conclusion, the presence of HA nanoparticles significantly enhanced osteogenic differentiation, indicated by increased calcium deposition. This effect is consistent with HA's known role in promoting hMSC osteogenesis and bone formation. *M* scaffolds showed higher ALP activity and calcium deposition than *S* scaffolds at Day 21, possibly due to greater cell spreading and more pronounced vinculin expression in *M* scaffolds **(Figure 7)**. Cell-matrix interactions and the spread cell morphology, associated with integrin-binding (vinculin), activate mechanotransduction pathways (Rho kinase and focal adhesion kinase) involved in osteogenesis, ultimately enhancing stem cell differentiation.[92-95]

Conclusions

1- In this study, we investigated the effects of melt-based and solution-based printing on the properties of scaffolds and their impact on in vitro bone formation, focusing on PCL/HA composites, a widely used system in bone tissue engineering. While HA is the most commonly used particle, there is a range of alternative particles that can also be explored. We are currently investigating the use of TCP and various human bone-derived particles, and the promising results from this work will be submitted in a forthcoming manuscript. The key findings of this study are as follows:

1- Scaffold morphology and structure: Melt-based printing produced smooth, solid struts, while solution-based printing in a nonsolvent bath resulted in rough struts with internal porosity. These differences in strut morphology directly influenced scaffold properties.
2- Material properties: Scaffolds fabricated through solution-based printing exhibited significantly higher polymer crystallinity. The incorporation of HA nanoparticles increased both the crystallinity percentage and decreased the thermal decomposition temperature. In contrast, melt-printed scaffolds, despite having lower overall crystallinity, were significantly stiffer. The addition of HA nanoparticles further enhanced the stiffness of these scaffolds.
3- Stem cell behaviour: hMSCs cultured on melt-printed scaffolds showed enhanced cellular spreading and more pronounced focal adhesions (evidenced by vinculin staining), which promoted osteogenic differentiation and bone formation. These cell-matrix interactions were more effective in directing stem cell fate towards osteogenesis on melt-printed scaffolds.

This study addresses a critical gap in the literature by examining how the printing process influences scaffold properties and bone regeneration. Our findings underscore the importance of scaffold architecture and material composition in guiding stem cell behaviour, offering valuable insights for designing scaffolds tailored to bone tissue engineering. By demonstrating the superior performance of melt-printed composite scaffolds in enhancing bone formation, this work provides key guidance for optimizing 3D printing techniques to advance bone tissue engineering applications.

Experimental

Materials

PCL (MW= 80,000 g/mol), HA powder (nanopowder, <200 nm particle size (BET), ≥97%, synthetic), THF, EtOH, and acetone were obtained from Sigma Aldrich. All materials are used as received.

Ink formulation

For melt-based printing, PCL pellets were kept under vacuum overnight prior to printing. PCL/HA composites were prepared by dissolving PCL pellets with HA particles (80:20 weight ratio) in acetone and stirring the solution at 45°C in a sealed vial overnight to create a homogenous HA suspension in PCL solution. The suspension was poured into a glass petri dish and kept under vacuum to remove acetone. The resulting dry film was cut into smaller pieces and kept under vacuum prior to printing. SEM was used to confirm homogenous particle dispersion within composite films. For melt printing, PCL pellets and PCL/HA composite formulations are referred as N-M (neat-melt) and C-M (composite-melt), respectively. For solution-based printing, a 26% (w/v) PCL solution was prepared in tetrahydrofuran (THF), which was stirred at 45°C overnight in a sealed vial to ensure formation of a homogenous solution. To prepare the composite ink, HA powder was suspended in excess THF, PCL particles were dissolved at 45°C maintaining a PCL/HA weight ratio of 80:20. The excess THF was evaporated at 45°C while continuously stirring in a chemical hood while adjusting the final PCL content to 26% (w/v). Neat PCL and PCL/HA composite solutions were coded as N-S (neat-solution) and C-S (composite-solution), respectively.

3D printing of scaffolds

A 4-layer disk-shaped scaffold featuring a grid pattern, i.e., a linear infill pattern (0.75 mm spacing) with alternating 0° and 90° rotation between layers, was designed using Autodesk® Fusion 360™ software. The scaffold (1 mm in height and 14 mm in diameter) was designed to fit in a 24-well plate. Repetier software (Hot-World GmbH & Co. KG) was used to create a digitally sliced (250 μm in layer height) gcode file for printing. Bioplotter® Starter Series (EnvisionTEC GmbH, Germany) was used for melt-based printing. An Allevi 2 printer (3D Systems) placed in a chemical hood was used for solvent-based printing.

For melt-printing, PCL pellets and PCL/HA composite formulation were kept under vacuum overnight, transferred into stainless-steel syringes, heated to a printing temperature (150°C for PCL and 180°C for PCL/HA), and printed onto a glass coverslip. A built-in line test protocol for Bioplotter® printer was used to determine the optimum printing parameters, including temperature, pressure, and speed. Briefly, print nozzle made a single pass at a nozzle offset (nozzle tip to print surface distance) equal to nozzle diameter (400 μm) creating individual struts using a range of print pressures and speeds at a predefined print temperature. Optical and scanning electron microscopy (SEM) images were used to determine the strut width and height. Print parameters were optimized to print struts with a 200 μm diameter. For solution-printing, ink formulations were loaded into a syringe, print needle was fully immersed in an ethanol, a nonsolvent for PCL, bath at room temperature. Scaffolds were printed onto coverslips, gently removed from the bath, and dried in the chemical hood. Like melt-printing, line test was performed to determine the optimum print pressure and speed to create print struts with ~200 μm diameter. Here, strut size was measured immediately after printing and post-drying to determine the shrinkage. The printed strut size was adjusted to compensate for the shrinkage to create scaffolds that are similar in size and shape when compared to scaffolds fabricated by melt-printing.

Characterization of scaffolds

Scaffold structure. Optical microscopy, SEM (JSM-7900F, JEOL, Tokyo, Japan), and micro computed tomography (Micro-CT, SkyScan 1275, Bruker, Billerica, MA, USA) were used for structural analysis. SEM was performed at an acceleration of 5.0 kV at 50x and 250x magnification for samples coated with Pd/Au (10 nm) to measure the strut size and the strut-to-strut distance. Micro-CT was used to measure the porosity of the scaffolds and struts. After the image acquisition step, the images were

reconstructed in NRecon (Bruker) creating 3D images from top and cross-sectional views to evaluate scaffold and strut porosity using CTAn softeware (Bruker). SEM images of the struts were also used to calculate porosity using ImageJ.

Thermal Analysis. Thermal behaviour of scaffolds was evaluated by thermogravimetric analysis (TGA, Perkin Elmer 8000, Inc., MA, USA) and differential scanning calorimeter (DSC, 6000 DSC from PerkinElmer, Inc., MA, USA). For this purpose, samples were randomly cut from top, centre and bottom regions of the scaffolds. In TGA, samples (10-15mg) underwent a heating cycle from room temperature to 500°C, at a rate of 10°C/min, within a nitrogen gas environment with a purge rate of 60mL/min. DSC was used to determine polymer melting point, crystallization temperature, and percent (%) crystallinity. Samples (7-9 mg) were placed in an aluminium pan and subjected heating from 0°C to 250°C at a rate of 10°C/min under nitrogen gas. The first heating cycle was recorded to investigate the influence of the printing process on the thermal history of the 3D printed scaffolds. The crystallinity of the scaffolds was calculated using the following equation:

$$\boldsymbol{X_c = \frac{\Delta H_m}{w \Delta H_m^\circ} x100}$$

Here, $\boldsymbol{\Delta H_m (Jg^{-1})}$ is the enthalpy obtained by integrating the area under the melting peak, *w* is the PCL weight fraction, and $\boldsymbol{\Delta H_m^\circ}$ is the heat of fusion, equal to 136 $\boldsymbol{Jg^{-1}}$ for 100% crystalline PCL.[96-98]

Mechanical Behaviour. Tensile tests were performed in an MTS Criterion Model 43 (MTS Systems Corporation) with displacement control using a 1.4 kg (2.5-pound) load cell (Transducer Techniques MDB-2.5). Individual struts (filaments) were printed onto a grid pattern, carefully peeled off the surface, and tested to evaluate the stiffness of the 3D-printed polymers. Samples (60 mm in length) were secured to a paper guide using superglue (30 mm gauge length, 15 mm grip length), and strained at a crosshead speed of 1 mm/min until necking occurred. Samples were tested at room temperature (24 °C) in accordance with ASTM D3822 standard. The engineering strain was measured using the non-contact Digital Image Correlation (DIC) software Vic2D (Correlated Solutions), which is integrated with a digital camera (Point Grey GRAS-50S5M-C). To create contrast for imaging, a white paint was applied to the grip. Tensile modulus (stiffness) of the struts was calculated as the slope of the linear region in the stress-strain curve (n = 3 per condition).

Surface roughness. Atomic force microscope (AFM, Dimension ICON, Bruker) equipped with a silicon nitride probe (with 10 nm nominal radius of curvature) was used in tapping mode to obtain surface topography scans. ScanAsyst mode (Bruker) using a probe tip (RFESP-75, Bruker) with rectangular geometry and a nominal spring constant of 0.30 N/m was used. 3D printed filaments for all conditions were prepared by cutting them into 1 cm x 1 cm sections and mounting them on a glass slide and securing them with an adhesive tape. Average surface roughness (R_a) and root-mean-square roughness (R_q) were reported for 3 replicates per condition.

Cell culture and characterization

Preparation of scaffolds for cell culture. Scaffolds were immersed in a 75% ethanol solution for 1 h, transferred into a biohood, rinsed with Dulbecco's Phosphate Buffered Saline (DPBS, Gibco) three times, dried in the biohood for 30 min, and exposed to irradiation with a germicidal UV lamp for 1 h on each side. Each scaffold was incubated in a 300 µL fibronectin solution (20 µg/mL, bovine fibronectin plasma, Invitrogen) overnight under gentle shaking to facilitate cell adhesion. The scaffolds were rinsed with DPBS, transferred into 24-well plates (untreated) containing stem cell growth media (covering the scaffolds), and incubated in a cell culture incubator until the cells were seeded.

Cell culture. Human mesenchymal stem cells (hMSCs, passage 4, Lonza, Walkersville, MD, USA) were cultured in growth media composed of α-MEM (minimum essential medium) supplemented with 10% fetal bovine serum (FBS, Gibco, New York, NY, USA) and 1% penicillin-streptomycin (pen-strep, Gibco, New York, NY, USA). The hMSCs were seeded on to the scaffolds (300 µL per scaffold corresponding to 10,000 cells/cm^2) and allowed to attach to the scaffolds while incubating at 37°C for 60 min. The scaffolds were then placed into a new untreated 24-well plates, and 1 mL of fresh GM was added into each well. The cells were cultured for 14 days in GM. For osteogenic differentiation studies, GM was replaced with hMSC osteogenic differentiation medium (OM, OM BulletKit™, Lonza, Basel, Switzerland) on Day 7, and the cells were cultured for an additional 14 days (21 days total) in OM. Media was refreshed every 3 days during cell culture experiments.

Cell viability and proliferation. An AlamarBlue™ assay (Invitrogen) and a PicoGreen™ assay (Quant-iT™ PicoGreen™ dsDNA Assay Kit, Invitrogen) were used for cell viability and proliferation on culture days 1, 4, 7, and 14 (6 samples per condition) in GM. For PicoGreen™ assay, cells from each sample group were lysed, collected, and stored at −80°C until all time points were collected for quantification. For both assays, a Tecan plate reader (Infinite M200 Pro, Tecan, Männedorf, Switzerland) was used. To visualize adherent stem cells on the scaffolds, cells were stained for F-actin and nuclei. Scaffolds were washed with DPBS (3x), incubated in 4% formaldehyde for 15 min, and washed with DPBS (3x). Cell membrane was permeabilized in 0.25% Triton-X in DPBS for 1 h. Rhodamine phalloidin staining (1:40 in DPBS, Invitrogen) was used for F-actin. Cell nuclei were stained with 4′,6-diamidino-2-phenylindole (DAPI, 1:2000 in DPBS, Sigma, St. Louis, MO, USA).

Osteogenic differentiation. Alkaline phosphatase (ALP) activity was assessed at day 14, using the QuantiChrom™ Alkaline Phosphatase Assay Kit (ALP assay Kit, BioAssay Systems, Hayward, NY, USA). Cells within the scaffolds were lysed with 0.2% Triton-X and incubated with p-nitrophenyl phosphate solution. The solution was scanned at 405 nm using a Tecan plate reader. Calcium deposition on the scaffolds was studied for cells

cultured for 21 days using an alizarin red (AR) staining kit (Sigma, St. Louis, MO, USA). After staining, cells were washed three times with DPBS and treated with 10% cetylpyridinium chloride (Sigma, St. Louis, MO, USA) in sodium phosphate buffer (10 mM, pH 7, Sigma) to remove the stain from scaffolds for quantification using a Tecan plate reader (scanning at 562 nm). Immunostaining was done to visualize vinculin (Day 7) and osteocalcin (OC, Day 21) using an anti-vinculin-FITC antibody (1:50, mouse monoclonal, Sigma) and OC primary antibody (1:200, monoclonal mouse, Invitrogen), respectively. For immunostaining, scaffolds were incubated in a 10% goat serum (in PBS) for 30 min, rinsed (3x) in a staining solution (3% bovine serum albumin (BSA) + 0.1% Tween-20 + 0.25% Triton-X), and incubated overnight with antibody solution at 4°C. Cells were then incubated in an Alexa Fluor 488 rabbit anti-mouse secondary antibody (1:100, Invitrogen) at room temperature for 2 h. Cells were also stained with phalloidin (rhodamine phalloidin, Invitrogen) and DAPI to visualize F-actin and cell nuclei, respectively. Fluorescent imaging was conducted using confocal and multiphoton microscopy (TCS SP8 MP, Leica, Wetzlar, Germany). ImageJ (NIH, Bethesda, MD, USA) was used to analyse collected images.

Statistical analysis. The data were analysed using Prism 10 (Prism 10.1.1, GraphPad) and were presented as mean values along with their corresponding standard deviations for $n \geq 3$ samples (unless otherwise specified). To compare between different conditions, an analysis of variance (ANOVA) with Tukey's test with a confidence level of 95% was used. Statistical significance was determined at a p-value < 0.05.

Author Contributions

Conceptualization, methodology: H.G., A.A., C-Y.L., and M.G. Formal analysis, investigation, validation: H.G., A.A., E.C., C-Y.L., and K.A. Writing—review and editing: H.G., A.A., S.A.C, and M.G. Resources: S.A.C., and M.G. Software: H.G. and A.A. Supervision: S.A.C. and M.G. Visualization: H.G. and A.A. Writing—original draft: H.G., A.A., and M.G.

Conflicts of interest

There are no conflicts to declare.

Acknowledgements

This study is partially funded by the National Science Foundation Award Number 1714882, and by a funding from New Jersey Health Foundation (NJHF).

References

1. G. L. Koons, M. Diba and A. G. Mikos, *Nature Reviews Materials*, 2020, **5**, 584-603.
2. N. Xue, X. Ding, R. Huang, R. Jiang, H. Huang, X. Pan, W. Min, J. Chen, J. A. Duan, P. Liu and Y. Wang, *Pharmaceuticals (Basel)*, 2022, **15**.
3. D. W. Hutmacher, *Biomaterials*, 2000, **21**, 2529-2543.
4. T. M. Koushik, C. M. Miller and E. Antunes, *Advanced Healthcare Materials*, 2023, **12**, 2202766.
5. S. S. Lee, X. Du, I. Kim and S. J. Ferguson, *Matter*, 2022, **5**, 2722-2759.
6. F. J. O'Brien, *Materials Today*, 2011, **14**, 88-95.
7. J. Venugopal, P. Vadgama, T. S. Kumar and S. Ramakrishna, *Nanotechnology*, 2007, **18**, 055101.
8. A. Autissier, C. L. Visage, C. Pouzet, F. Chaubet and D. Letourneur, *Acta Biomaterialia*, 2010, **6**, 3640-3648.
9. Y. Zhang, F. Yang, K. Liu, H. Shen, Y. Zhu, W. Zhang, W. Liu, S. Wang, Y. Cao and G. Zhou, *Biomaterials*, 2012, **33**, 2926-2935.
10. M. Z. Moghadam, S. Hassanajili, F. Esmaeilzadeh, M. Ayatollahi and M. Ahmadi, *Journal of the mechanical behavior of biomedical materials*, 2017, **69**, 115-127.
11. A. Prasad, M. R. Sankar and V. Katiyar, *Materials Today: Proceedings*, 2017, **4**, 898-907.
12. Y. Ren, C. Zhang, Y. Liu, W. Kong, X. Yang, H. Niu, L. Qiang, H. Yang, F. Yang, C. Wang and J. Wang, *ACS Biomaterials Science & Engineering*, 2024, **10**, 255-270.
13. A. Wubneh, E. K. Tsekoura, C. Ayranci and H. Uludağ, *Acta Biomaterialia*, 2018, **80**, 1-30.
14. Y. S. Zhang, K. Yue, J. Aleman, K. Mollazadeh-Moghaddam, S. M. Bakht, J. Yang, W. Jia, V. Dell'Erba, P. Assawes and S. R. Shin, *Annals of biomedical engineering*, 2017, **45**, 148-163.
15. A. Abaci, G. Camci-Unal, and M. Guvendiren, *MRS Bulletin*, 2023, **48**, 624-631.
16. T. Lu, Y. Li and T. Chen, *International journal of nanomedicine*, 2013, 337-350.
17. A. P. Moreno Madrid, S. M. Vrech, M. A. Sanchez and A. P. Rodriguez, *Materials Science and Engineering: C*, 2019, **100**, 631-644.
18. A. Kumar, S. Mandal, S. Barui, R. Vasireddi, U. Gbureck, M. Gelinsky and B. Basu, *Materials Science and Engineering: R: Reports*, 2016, **103**, 1-39.
19. K. Prem Ananth and N. D. Jayram, *Annals of 3D Printed Medicine*, 2024, **13**, 100141.
20. R. Belluomo, A. Khodaei and S. Amin Yavari, *Acta Biomaterialia*, 2023, **156**, 234-249.
21. M.-M. Germaini, S. Belhabib, S. Guessasma, R. Deterre, P. Corre and P. Weiss, *Progress in Materials Science*, 2022, **130**, 100963.
22. P. Awasthi and S. S. Banerjee, *Additive Manufacturing*, 2021, **46**, 102177.
23. A. Haryńska, J. Kucinska-Lipka, A. Sulowska, I. Gubanska, M. Kostrzewa and H. Janik, *Materials*, 2019, **12**, 887.
24. Z. Jiao, B. Luo, S. Xiang, H. Ma, Y. Yu and W. Yang, *Advanced Industrial and Engineering Polymer Research*, 2019, **2**, 196-202.
25. M. Saadi, A. Maguire, N. T. Pottackal, M. S. H. Thakur, M. M. Ikram, A. J. Hart, P. M. Ajayan and M. M. Rahman, *Advanced Materials*, 2022, **34**, 2108855.

26. B. Zhang, S. H. Chung, S. Barker, D. Craig, R. J. Narayan and J. Huang, *Progress in Natural Science: Materials International*, 2021, **31**, 180-191.
27. B. Zhang, A. K. Nguyen, R. J. Narayan and J. Huang, *Journal of the American Ceramic Society*, 2022, **105**, 1821-1840.
28. L. Elomaa, E. Keshi, I. M. Sauer and M. Weinhart, *Materials Science and Engineering: C*, 2020, **112**, 110958.
29. J. Z. Manapat, Q. Chen, P. Ye and R. C. Advincula, *Macromolecular Materials and Engineering*, 2017, **302**, 1600553.
30. E. M. Maines, M. K. Porwal, C. J. Ellison and T. M. Reineke, *Green Chemistry*, 2021, **23**, 6863-6897.
31. G. Zhu, Y. Hou, J. Xu and N. Zhao, *Macromolecular Rapid Communications*, 2022, **43**, 2200053.
32. A. Kafle, E. Luis, R. Silwal, H. M. Pan, P. L. Shrestha and A. K. Bastola, *Polymers*, 2021, **13**, 3101.
33. A. Mazzoli, C. Ferretti, A. Gigante, E. Salvolini and M. Mattioli-Belmonte, *Rapid prototyping journal*, 2015, **21**, 386-392.
34. S. Gómez, M. D. Vlad, J. López and E. Fernández, *Acta Biomaterialia*, 2016, **42**, 341-350.
35. M. Cavo and S. Scaglione, *Materials Science and Engineering: C*, 2016, **68**, 872-879.
36. Y. S. Cho, S. J. Gwak and Y. S. Cho, *Polymers (Basel)*, 2021, **13**.
37. M. N. Collins, G. Ren, K. Young, S. Pina, R. L. Reis and J. M. Oliveira, *Advanced Functional Materials*, 2021, **31**, 2010609.
38. P. Camacho, M. Fainor, K. B. Seims, J. W. Tolbert and L. W. Chow, *J Biol Methods*, 2021, **8**, e146.
39. S. C. Altıparmak, V. A. Yardley, Z. Shi and J. Lin, *Journal of Manufacturing Processes*, 2022, **83**, 607-636.
40. C.-Y. Liaw and M. Guvendiren, *Biofabrication*, 2017, **9**, 024102.
41. M. Guvendiren, J. Molde, R. M. D. Soares and J. Kohn, *ACS Biomaterials Science & Engineering*, 2016, **2**, 1679-1693.
42. S. Ji, K. Dube, J. P. Chesterman, S. L. Fung, C.-Y. Liaw, J. Kohn and M. Guvendiren, *Biomaterials Science*, 2019, **7**, 560-570.
43. S. Ji and M. Guvendiren, *Micromachines*, 2020, **11** (1)**,** 31.
44. G. L. Koons, P. D. Kontoyiannis, M. Diba, L. K. Chim, D. W. Scott and A. G. Mikos, *Annals of Biomedical Engineering*, 2021, **49**, 2114-2125.
45. S.-Z. Guo, M.-C. Heuzey and D. Therriault, *Langmuir*, 2014, **30**, 1142-1150.
46. J.-M. Chen, D. Lee, J.-W. Yang, S.-H. Lin, Y.-T. Lin and S.-J. Liu, *Applied Sciences*, 2020, **10**, 3189.
47. S.-Z. Guo, F. Gosselin, N. Guerin, A.-M. Lanouette, M.-C. Heuzey and D. Therriault, *Small*, 2013, **9**, 4118-4122.
48. R. Karyappa, H. Liu, Q. Zhu and M. Hashimoto, *ACS Applied Materials & Interfaces*, 2023, **15**, 21575-21584.
49. J. W. Tolbert, T. French, A. Kitson, C. Okpara, D. E. Hammerstone, S. Lazarte, T. F. Babuska, T. Gonzalez-Fernandez, B. A. Krick and L. W. Chow, *Journal of Biomedical Materials Research Part A*, 2024, **112**, 1364-1375.
50. B. Zhang, R. Cristescu, D. B. Chrisey and R. J. Narayan, *Int J Bioprint*, 2020, **6**, 211.
51. A. Abaci, C. Gedeon, A. Kuna and M. Guvendiren, *Pharmaceutics*, 2021, **13** (2), 156.
52. A. House, A. Kuna, D. Hastings, N. Rodriguez, M. Schoenitz, E. L. Dreizin and M. Guvendiren, *Progress in Additive Manufacturing*, 2023, **8**, 1573-1585.
53. J. M. Seok, T. Rajangam, J. E. Jeong, S. Cheong, S. M. Joo, S. J. Oh, H. Shin, S.-H. Kim and S. A. Park, *Journal of Materials Chemistry B*, 2020, **8**, 951-960.
54. D. Gao, Z. Wang, Z. Wu, M. Guo, Y. Wang, Z. Gao, P. Zhang and Y. Ito, *Materials Science and Engineering: C*, 2020, **112**, 110942.
55. X. Hu, Z. Yang, S. Kang, M. Jiang, Z. Zhou, J. Gou, D. Hui and J. He, 2020, **9**, 345-353.
56. J. W. Kim, K. H. Shin, Y. H. Koh, M. J. Hah, J. Moon and H. E. Kim, *Materials (Basel)*, 2017, **10**.
57. K.-H. Shin, I.-H. Jo, S.-E. Kim, Y.-H. Koh and H.-E. Kim, *Materials Letters*, 2014, **122**, 348-351.
58. J. Search, A. Mahjoubnia, A. C. Chen, H. Deng, A. J. Tan, S.-y. Chen and J. Lin, *Additive Manufacturing*, 2023, **68**, 103514.
59. K.-H. Shin, J.-W. Kim, Y.-H. Koh and H.-E. Kim, *Materials Letters*, 2015, **143**, 265-268.
60. A. V. Mironov, O. A. Mironova, M. A. Syachina and V. K. Popov, *Polymer*, 2019, **182**, 121845.
61. M. S. Aydin, M. Sahin, Z. Dogan and G. Kiziltas, *ACS Omega*, 2023, **8**, 47595-47605.
62. J.-W. Choi, W.-Y. Maeng, Y.-H. Koh, H. Lee and H.-E. Kim, *Journal*, 2019, **12**.
63. Z. U. Arif, M. Y. Khalid, R. Noroozi, A. Sadeghianmaryan, M. Jalalvand and M. Hossain, *International Journal of Biological Macromolecules*, 2022, **218**, 930-968.
64. E. H. Backes, S. V. Harb, C. A. G. Beatrice, K. M. B. Shimomura, F. R. Passador, L. C. Costa and L. A. Pessan, *Journal of Biomedical Materials Research Part B: Applied Biomaterials*, 2022, **110**, 1479-1503.
65. R. Dwivedi, S. Kumar, R. Pandey, A. Mahajan, D. Nandana, D. S. Katti and D. Mehrotra, *Journal of Oral Biology and Craniofacial Research*, 2020, **10**, 381-388.
66. M. P. Nikolova and M. S. Chavali, *Bioactive Materials*, 2019, **4**, 271-292.
67. M. A. Woodruff and D. W. Hutmacher, *Progress in Polymer Science*, 2010, **35**, 1217-1256.
68. S. Park, J. E. Kim, J. Han, S. Jeong, J. W. Lim, M. C. Lee, H. Son, H. B. Kim, Y. H. Choung, H. Seonwoo, J. H. Chung and K. J. Jang, *Polymers (Basel)*, 2021, **13**.
69. P. S. P. Poh, D. W. Hutmacher, B. M. Holzapfel, A. K. Solanki, M. M. Stevens and M. A. Woodruff, *Acta Biomaterialia*, 2016, **30**, 319-333.
70. A. Zimmerling, Z. Yazdanpanah, D. M. L. Cooper, J. D. Johnston and X. Chen, *Biomaterials Research*, 2021, **25**, 3.
S. Naghieh and X. Chen, *Journal of Pharmaceutical Analysis*, 2021, **11**, 564-579.
72. M. Guvendiren and J. A. Burdick, *Biomaterials*, 2010, **31**, 6511-6518.

73. J. Xia, Y. Yuan, H. Wu, Y. Huang and D. A. Weitz, *Biomaterials*, 2020, **248**, 120014.
74. Y. Hou, W. Xie, L. Yu, L. C. Camacho, C. Nie, M. Zhang, R. Haag and Q. Wei, *Small*, 2020, **16**, 1905422.
75. Kshitiz, J. Park, P. Kim, W. Helen, A. J. Engler, A. Levchenko and D. H. Kim, *Integr Biol (Camb)*, 2012, **4**, 1008-1018.
76. S. Biscaia, M. V. Branquinho, R. D. Alvites, R. Fonseca, A. C. Sousa, S. S. Pedrosa, A. R. Caseiro, F. Guedes, T. Patrício, T. Viana, A. Mateus, A. C. Maurício and N. Alves, *International Journal of Molecular Sciences*, 2022, **23**, 2318.
77. B. Zhang, L. Wang, P. Song, X. Pei, H. Sun, L. Wu, C. Zhou, K. Wang, Y. Fan and X. Zhang, *Materials & Design*, 2021, **201**, 109490.
78. B. Huang, Y. Wang, C. Vyas and P. Bartolo, *Advanced Science*, 2023, **10**, 2203183.
79. S. A. Ghodbane, N. S. Murthy, M. G. Dunn and J. Kohn, *Biofabrication*, 2019, **11**, 045004.
80. C. McIlroy and R. S. Graham, *Additive Manufacturing*, 2018, **24**, 323-340.
81. B. Nazari, A. M. Rhoades, R. P. Schaake and R. H. Colby, *ACS Macro Lett*, 2016, **5**, 849-853.
82. M. Guvendiren and J. A. Burdick, *Nature Communications*, 2012, **3**, 792.
83. R. J. Pelham and Y.-l. Wang, *Proceedings of the National Academy of Sciences*, 1997, **94**, 13661-13665.
84. M. Sun, G. Chi, P. Li, S. Lv, J. Xu, Z. Xu, Y. Xia, Y. Tan, J. Xu, L. Li and Y. Li, *Int J Med Sci*, 2018, **15**, 257-268.
85. J. Swift, I. L. Ivanovska, A. Buxboim, T. Harada, P. D. P. Dingal, J. Pinter, J. D. Pajerowski, K. R. Spinler, J.-W. Shin and M. Tewari, *Science*, 2013, **341**, 1240104.
86. K. H. Vining and D. J. Mooney, *Nat Rev Mol Cell Biol*, 2017, **18**, 728-742.
87. R. G. Wells, *Hepatology*, 2008, **47**, 1394-1400.
88. J. Nam, J. Johnson, J. J. Lannutti and S. Agarwal, *Acta Biomater*, 2011, **7**, 1516-1524.
89. A. Y. Al-Maharma, S. P. Patil and B. Markert, *Materials Research Express*, 2020, **7**, 122001.
90. C.-Y. Liaw, J. W. Tolbert, L. W. Chow and M. Guvendiren, *Soft Matter*, 2021, **17**, 4775-4789.
91. Z. Ebrahimi, S. Irani, A. Ardeshirylajimi and E. Seyedjafari, *Scientific Reports*, 2022, **12**, 12359.
92. R. McBeath, D. M. Pirone, C. M. Nelson, K. Bhadriraju and C. S. Chen, *Developmental Cell*, 2004, **6**, 483-495.
93. R. M. Salasznyk, R. F. Klees, W. A. Williams, A. Boskey and G. E. Plopper, *Experimental Cell Research*, 2007, **313**, 22-37.
94. Y.-R. V. Shih, K.-F. Tseng, H.-Y. Lai, C.-H. Lin and O. K. Lee, *Journal of Bone and Mineral Research*, 2011, **26**, 730-738.
95. M. D. Treiser, E. H. Yang, S. Gordonov, D. M. Cohen, I. P. Androulakis, J. Kohn, C. S. Chen and P. V. Moghe, *Proc Natl Acad Sci U S A*, 2010, **107**, 610-615.
96. V. Crescenzi, G. Manzini, G. Calzolari and C. Borri, *European Polymer Journal*, 1972, **8**, 449-463.
97. F. B. Khambatta, F. Warner, T. Russell and R. S. Stein, *Journal of Polymer Science: Polymer Physics Edition*, 1976, **14**, 1391-1424.
98. M. Nagata and Y. Yamamoto, *Journal of Polymer Science Part A: Polymer Chemistry*, 2009, **47**, 2422-2433.

Data (csv and tiff/jpeg) will be available publicly through google drive share.
https://drive.google.com/drive/folders/1gW1_9zXsVAuErERt8lijca9gEoPB2PQh?usp=share_link